

Seasonal Modulations in the Eddy Field of the South Pacific Ocean

BO QIU AND SHUIMING CHEN

Department of Oceanography, University of Hawaii at Manoa, Honolulu, Hawaii

(Manuscript received 25 July 2003, in final form 4 December 2003)

ABSTRACT

Decade-long satellite altimeter data from the Ocean Topography Experiment (TOPEX)/Poseidon and *European Remote Sensing Satellite-1* and *-2* (ERS-1/2) missions are analyzed to investigate the eddy signals in the South Pacific Ocean. High-eddy kinetic energy (EKE) bands with well-defined annual cycles are detected along the eastward-flowing surface currents of the South Tropical Countercurrent (STCC) between 21°–29°S and the South Equatorial Countercurrent (SECC) centered near 9°S. Overriding the westward-flowing South Equatorial Current (SEC), the STCC layer has the sign of its mean potential vorticity gradient opposite to that in the SEC layer, subjecting the vertically sheared STCC–SEC system to baroclinic instability. In austral winter, the STCC–SEC system is baroclinically more unstable than in other seasons because of the large vertical shear and weak stratification. This seasonal variation in the intensity of baroclinic instability is responsible for the seasonal modulation of the STCC's EKE field with a November–December maximum and a June–July minimum. The large deformation radius in the low-latitude SECC region, on the other hand, prevents the vertically sheared SECC–SEC system from becoming baroclinically unstable. With the broad, westward-flowing SEC weakening the stabilizing planetary β effect, the high EKE level observed along the SECC is found to result from the barotropic instability associated with the horizontal shear of the SECC–SEC system. Together with an analysis of energetics, it is shown that the seasonal variation in the intensity of barotropic instability accounts for the seasonal modulation of the SECC's EKE field, with a maximum in April and a minimum in August.

1. Introduction

High-quality sea surface height measurements from the Ocean Topography Experiment (TOPEX)/Poseidon (T/P) and *European Remote Sensing Satellite* (ERS)-1/2 satellites over the past decade have provided the oceanography community with an unprecedented opportunity to study the variability of the world's ocean circulations [for a comprehensive review, see Fu and Cazenave (2001)]. In addition to being a useful means to monitor the global sea surface height field on a temporally repetitive basis, the decade-long altimeter data have also become instrumental in detecting new, time-varying circulation features in the ocean basins where systematic measurements have heretofore been limited. The South Pacific Ocean, with its broad geographic extent, is a good example of such a basin and it constitutes the focus of this study.

Figure 1 shows the distribution of the rms sea surface height (SSH) variability in the South Pacific Ocean derived from the combined T/P and ERS-1/2 altimeter data for the period from October 1992 to February 2002. Outside of the 5° equatorial band, high-variability re-

gions can be seen in 1) the zonal band of 6°–12°S along the South Equatorial Countercurrent (see Fig. 2), 2) the subtropical western boundary current (the East Australia Current), 3) the zonal band of 21°–29°S between 165°E and 130°W, and 4) the Southern Ocean along the Antarctic Circumpolar Current (ACC). While the high variability in the ACC and the western boundary current is dynamically expected, reasons for the existence of the high-variability zonal bands 1 and 3 are less obvious. The South Equatorial Countercurrent (SECC), for example, has been found consistently in the past to be a weak, surface-trapped zonal current (e.g., Reid 1959; Tsuchiya 1968; Kessler and Taft 1987; Delcroix et al. 1987; Gouriou and Toole 1993). Indeed, a look at the zonal geostrophic velocity profile based on the climatological temperature and salinity datasets of the *World Ocean Atlas 2001* (WOA01; Conkright et al. 2002) reveals that the SECC is a relatively narrow jet with a mean speed of $<10 \text{ cm s}^{-1}$ and confined to the surface 150-m layer (see Fig. 3).

The high-variability band 3 is located near the longitudinal center of the wind-driven South Pacific subtropical gyre (e.g., de Szoeke 1987), where one might normally expect low eddy activity. While the region in the 21°–29°S band corresponds to none of the commonly recognized currents presented in Fig. 2, Fig. 3 indicates that a shallow, eastward-flowing zonal current does exist

Corresponding author address: Dr. Bo Qiu, Department of Oceanography, University of Hawaii at Manoa, 1000 Pope Road, Honolulu, HI 96822.
E-mail: bo@soest.hawaii.edu

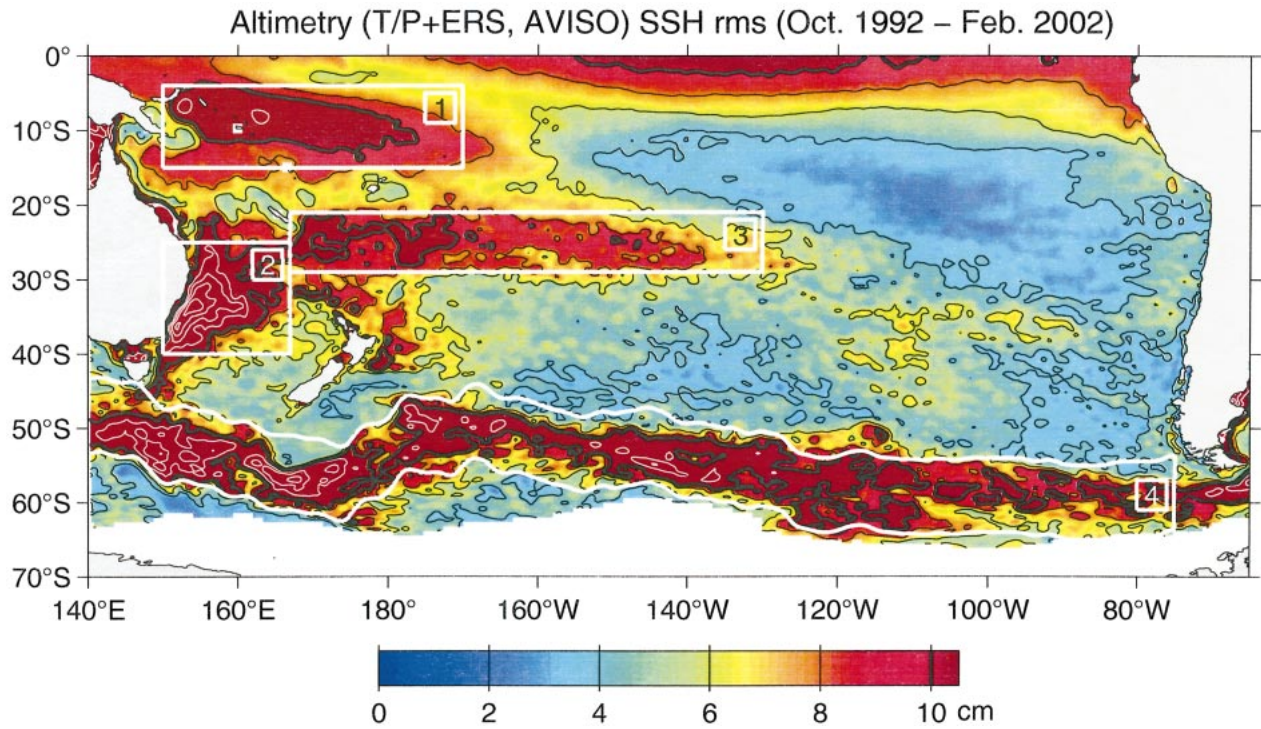


FIG. 1. Map of the rms sea surface height variability in the South Pacific Ocean. Based on the combined T/P and ERS-1/2 altimetric data from Oct 1992 to Feb 2002. Thick solid lines denote the 0.1-m contour. In regions above 0.1 m, thin white lines denote contours at a 0.05-m interval.

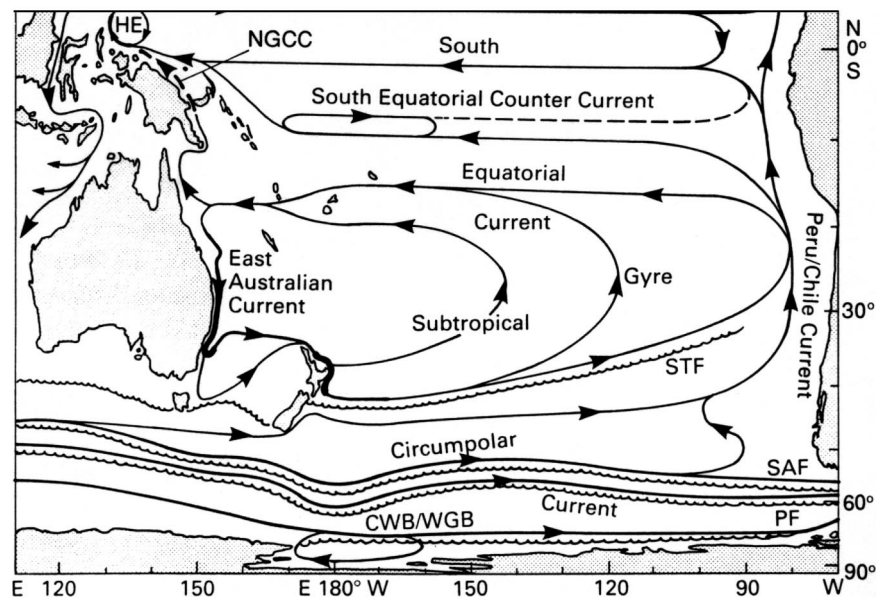


FIG. 2. Surface current system of the South Pacific Ocean from Tomczak and Godfrey (1994). Abbreviations in the figure are as follows: Halmahera Eddy (HE), New Guinea Coastal Current (NGCC), Subtropical Front (also called the South Pacific Current) (STF), subantarctic front (SAF), polar front (PF), and continental water boundary/Weddell gyre boundary (CWB/WGB).

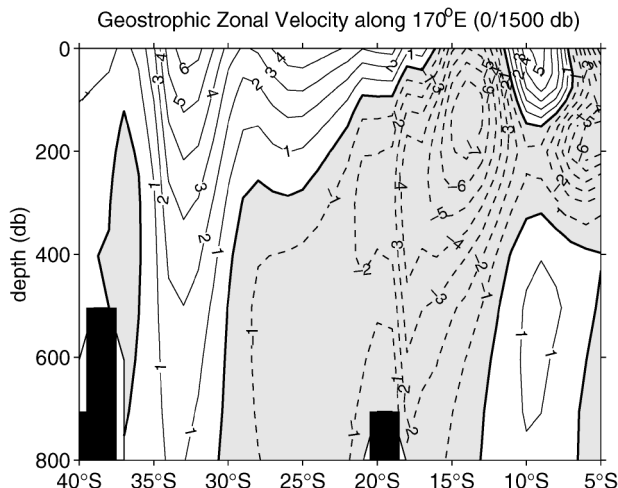


FIG. 3. Geostrophic zonal flow pattern along 170°E calculated from the annual mean temperature and salinity data sets of WOA01 (Conkright et al. 2002). The reference level is at 1500 dbar or at the bottom if the water depth is shallower. The solid contours are for eastward flows and the dashed ones in the shaded area are for westward flows. Contour units are centimeters per second.

in this band. This current was identified and named the South Tropical Countercurrent (STCC) in the study by Merle et al. (1969).¹ Although the STCC was found to be weak and variable in the original study by Merle et al., its existence as a *mean* eastward flowing current is well captured in the repeat high-resolution XBT measurements between New Zealand and Fiji by Roemmich and Cornuelle (1990) and Morris et al. (1996). Notice that in Fig. 3, the STCC can be seen above the 250-m depth, bordered to the north and underneath by the westward-flowing SEC and to the south, ~30°S, by the eastward-flowing extension of the East Australia Current (EAC). Because the STCC is located where the regional Ekman convergence is a maximum (see Fig. 4a in Huang and Qiu 1998), it is referred to in some literatures also as the South Pacific “tropical convergence” (de Szoeke 1987; Roemmich and Cornuelle 1990).

It is worth emphasizing that the STCC along the 21°–29°S band is *not* part of the eastward extension of the subtropical western boundary current, the EAC. In other words, the high rms variability in this zonal band revealed by the altimeter measurements (Fig. 1) is not a consequence of the high mesoscale eddy variability associated with the western boundary current extensions commonly found in the other subtropical ocean basins. As seen in Fig. 2, the EAC detaches from the Australian coast near 35°S and, after reaching the northern tip of

¹ With its existence in the wind-driven subtropical gyre of the South Pacific, a more appropriate nomenclature for the South Tropical Countercurrent (STCC) would have been the South Pacific Subtropical Countercurrent. Indeed, the correspondence between the STCC and the North Pacific Subtropical Countercurrent was pointed out by Rot-schi (1973). For historical reasons, however, the name of STCC will be used throughout this study.

New Zealand, it flows *poleward* along the New Zealand coast to form the East Auckland Current (Stanton et al. 1997; Roemmich and Sutton 1998). That the rms SSH variability associated with the STCC in the center of the subtropical gyre should be comparable to that of the western boundary current extension is a unique aspect of the South Pacific Ocean circulation.

The objective of this study is to examine and understand the eddy variability in the zonal bands of the SECC and the STCC. Following a brief description of the altimetric data in the next section, we will show that these two zonal bands exhibit an elevated level of eddy kinetic energy with highly regular annual cycles. In section 3, we will focus on the STCC and clarify mechanisms responsible for the generation and the seasonal modulation of its eddy kinetic energy field. Dynamic processes governing the seasonal evolution of the mean flow field of the SECC are discussed in section 4, and in section 5 we show how this evolution of the mean flow contributes to the observed seasonal modulation in the SECC’s eddy kinetic energy field. That the mechanism responsible for the seasonal modulation of the SECC’s eddy signals is dynamically different from that of the STCC is emphasized. Results of this study are summarized in section 5.

2. EKE field from altimeter measurements

For this study we use the global SSH anomaly dataset compiled by the CLS Space Oceanographic Division of Toulouse, France. The dataset merges the T/P and ERS-1/2 along-track SSH measurements for the period from October 1992 to February 2002. It has a 7-day temporal resolution and a $1/3^\circ \times 1/3^\circ$ spatial resolution. For the detailed mapping method and data quality analysis, readers are referred to Le Traon and Ogor (1998) and Le Traon et al. (1998). From the gridded SSH anomaly data $h'(x, y, t)$, it is straightforward to evaluate the eddy kinetic energy field:

$$\text{EKE} \equiv \frac{g^2}{2f^2} \left[\left(\frac{\partial h'}{\partial x} \right)^2 + \left(\frac{\partial h'}{\partial y} \right)^2 \right], \quad (1)$$

where g denotes the gravity constant and f is the Coriolis parameter.

Figure 4a shows the time series of the EKE averaged over the South Equatorial Countercurrent band of 5°–15°S and 150°E–170°W (see box 1 in Fig. 1). The time-mean eddy kinetic energy level in this band is 242 $\text{cm}^2 \text{s}^{-2}$, which is equivalent to an rms velocity anomaly of 15 cm s^{-1} . Given that the mean flow of the SECC is $<10 \text{ cm s}^{-1}$ (Fig. 3), this large rms velocity anomaly implies that the presence of a coherent SECC can be masked by eddies at any given instant. Indeed, studies based on repeat in situ measurements in the past have all stressed the “intermittent” nature of the SECC (Kessler and Taft 1987; Delcroix et al. 1987; Gouriou and Toole 1993). From Fig. 4a, it is clear that the eddy

kinetic energy of the SECC modulates on a seasonal time scale. Removing the interannual signals from Fig. 4a and plotting the remaining time series as a function of calendar month (Fig. 5a) reveals that the EKE in the SECC peaks in March–April and has a peak-to-peak amplitude $>100 \text{ cm}^2 \text{ s}^{-2}$. From Fig. 5a, a secondary EKE maximum can be seen in October, although its amplitude is much smaller than the dominant seasonal peak of March–April. In addition to the seasonal signals, interannual variability is also noticeable in the SECC's EKE field shown in Fig. 4a. For example, the EKE level is higher in 1998 and 1999 than the other years, and the seasonal EKE modulation appears to be more pronounced in the years following 1998.

Figure 4b shows the time series of the EKE averaged over the East Australia Current region of $25^\circ\text{--}40^\circ\text{S}$ and $150^\circ\text{--}167^\circ\text{E}$ (box 2 in Fig. 1). The time-mean EKE level in this region is $452 \text{ cm}^2 \text{ s}^{-2}$, which is comparable to the EKE levels in the Northern Hemisphere western boundary currents, the Gulf Stream and the Kuroshio Extension (cf. Ducet and Le Traon 2001). Interestingly, the EKE signal in the EAC exhibits an annual cycle quite similar in amplitude and phase to that of the SECC band (see Fig. 5b).

The most regular seasonal modulation of the EKE field is seen in the South Tropical Countercurrent band

of $21^\circ\text{--}29^\circ\text{S}$ and $167^\circ\text{E}\text{--}130^\circ\text{W}$ (Fig. 4c). The mean EKE level in this band is $172 \text{ cm}^2 \text{ s}^{-2}$, which translates to a rms velocity anomaly of 13 cm s^{-1} . As in the SECC, this rms velocity anomaly is much larger than the mean flow speed of the STCC ($\sim 5 \text{ cm s}^{-1}$; see Fig. 3). As shown in Fig. 5c, the peak-to-peak seasonal modulation has an amplitude close to $100 \text{ cm}^2 \text{ s}^{-2}$ and it has a maximum in November–December, as well as a well-defined minimum in June–July. Notice that this seasonal EKE cycle is nearly out-of-phase with that in the SECC band.

Figure 4d shows the EKE time series averaged over the 10° -wide band following the Antarctic Circumpolar Current from 140°E to 75°W (box 4 in Fig. 1). As shown in Fig. 5d, seasonal EKE modulation is barely discernible in this band. An interesting feature of Fig. 4d is the existence of a persistent and gradual increase in the EKE level in the ACC over the past 8 yr since 1994. The trend is roughly linear at a rate of $5.4 \text{ cm}^2 \text{ s}^{-2} \text{ yr}^{-1}$.

The decade-long SSH measurements by the satellite altimeters have presented us with a wide spectrum of the EKE changes in the high-variability regions of the South Pacific Ocean. In the following analyses, we will restrict our attention to the seasonal EKE modulations in the SECC and STCC regions with the belief that a solid understanding of the seasonal signals in these regions will provide valuable insights for future studies emphasizing the EKE signals on longer time scales.

3. Seasonal EKE modulation in the STCC

By analyzing hydrographic data along 170°E , Rotschi (1973) was the first to point out the similarity in the near-surface thermal structure between the STCC in the South Pacific and the Subtropical Countercurrent in the North Pacific (hereinafter NPSTCC; Yoshida and Kidokoro 1967). The similarity between these two eastward-flowing countercurrents, in fact, goes beyond their geographical locations and thermal structures. Using the T/P SSH data of 1992–97, Qiu (1999) found that the NPSTCC, characterized by high eddy variability in the zonal band $19^\circ\text{--}25^\circ\text{N}$ of the North Pacific subtropical gyre, also has a well-defined seasonal modulation of its EKE field. To understand this EKE modulation, Qiu (1999) adopted a $2\frac{1}{2}$ -layer reduced-gravity model representing the vertically sheared NPSTCC–North Equatorial Current (NEC) system and explained the observed seasonal modulation in the NPSTCC's eddy field as reflecting the intensity of baroclinic instability.

Similar to the NPSTCC–NEC system in the North Pacific, the STCC in the South Pacific is underlain by the westward-flowing South Equatorial Current (SEC) (see Fig. 3). While the subsurface SEC has a relatively constant westward velocity ($\sim -2 \text{ cm s}^{-1}$), the strength of the surface STCC is strongly modulated by the seasonal surface wind and buoyancy forcings (Morris et al. 1996). In Fig. 6 (solid line), we plot the monthly values of the zonal velocity shear between the surface STCC

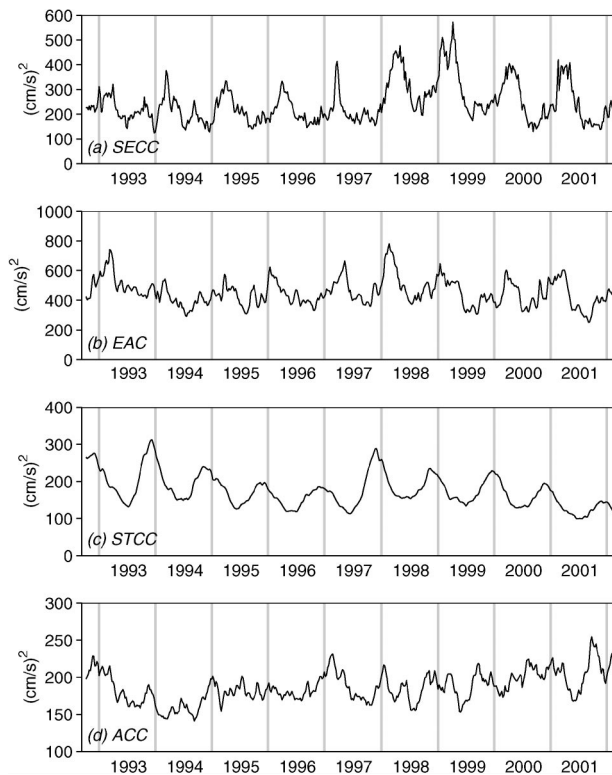


FIG. 4. Eddy kinetic energy averaged over each box in Fig. 1 as a function of time: (a) SECC, box 1; (b) EAC, box 2; (c) STCC, box 3; and (d) ACC, box 4. Notice that the y-axis scales are different among the panels.

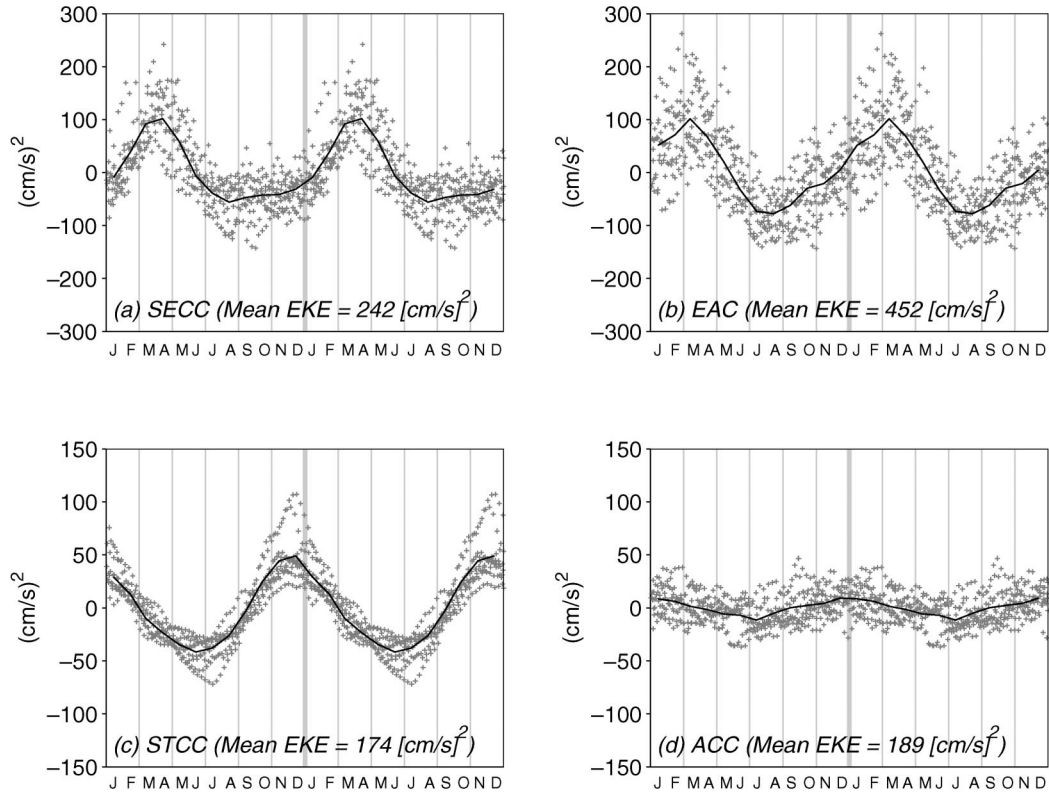


FIG. 5. Eddy kinetic energy as a function of calendar month in the (a) SECC, (b) EAC, (c) STCC, and (d) ACC regions. The EKE time series are derived from Fig. 4 using the third-order, high-pass Butterworth filter with a cutoff period of 2 yr. The filter is applied twice in the forward and reversed directions to avoid phase distortions. In each figure, crosses denote the high-pass filtered EKE values, and the solid line denotes their monthly averages.

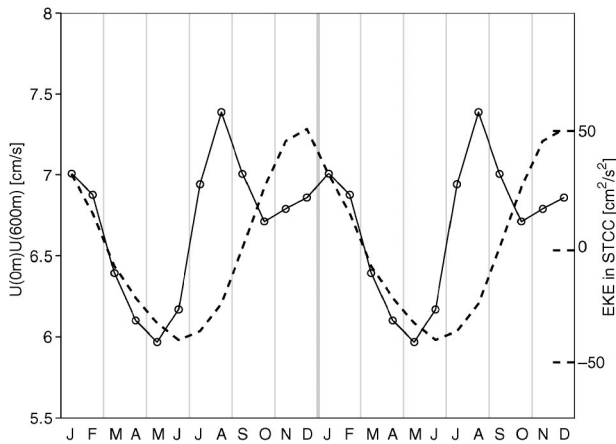


FIG. 6. Zonal velocity shear between 0 and 600 m averaged over the STCC–SEC region of 21°–29°S and 180°–160°W (solid line). The zonal flows are calculated from the monthly mean temperature and salinity datasets of WOA01 (Conkright et al. 2002) with a three-point smoothing (1/4, 1/2, 1/4) applied. The dashed line shows the monthly EKE time series in the STCC region (same as the solid line in Fig. 5c).

and SEC at the 600-m depth. The zonal velocity shear is largest in August when the surface cooling induced tilt of the seasonal thermocline reaches the maximum in late austral winter. The weakest shear is found in May when the surface ocean is capped by a flat and well-stratified seasonal thermocline due to the accumulative surface heating through austral summer. Also plotted in Fig. 6 (dashed line) are the seasonal EKE signals extracted from the satellite SSH measurements. Notice that the maximum STCC–SEC shear leads the EKE maximum by about 3 months.

To verify whether the seasonal EKE modulation observed in the South Pacific STCC band reflects the intensity of the baroclinic instability, we follow Qiu (1999) and consider the vertically sheared STCC–SEC system in the 2½-layer reduced-gravity model. Under the quasigeostrophic approximation, the linearized equations governing the perturbation potential vorticity q_n are

$$\left(\frac{\partial}{\partial t} + U_n \frac{\partial}{\partial x}\right)q_n + \frac{\partial \Pi_n}{\partial y} \frac{\partial \phi_n}{\partial x} = 0, \quad (2)$$

where ϕ_n is the perturbation streamfunction, U_n is the zonal mean velocity, and Π_n is the mean potential vorticity in layer n ($n = 1$ and 2 ; see Pedlosky 1987).

TABLE 1. Parameter values appropriate for the STCC–SEC system in Aug and May, and the SECC–SEC system in Mar. Dashes in the third column denote that the May value of the STCC–SEC system is the same as that of Aug.

Parameter	STCC–SEC: Aug	STCC–SEC: May	SECC–SEC: Mar
f_0	$-6.15 \times 10^{-5} \text{ s}^{-1}$	—	$-2.28 \times 10^{-5} \text{ s}^{-1}$
β	$2.08 \times 10^{-11} \text{ s}^{-1} \text{ m}^{-1}$	—	$2.27 \times 10^{-11} \text{ s}^{-1} \text{ m}^{-1}$
U_1	0.055 m s^{-1}	0.04 m s^{-1}	0.20 m s^{-1}
U_2	-0.02 m s^{-1}	—	0.02 m s^{-1}
H_1	200 m	—	200 m
H_2	700 m	—	300 m
ρ_1	$24.80 \sigma_\theta$	$24.4 \sigma_\theta$	$22.5 \sigma_\theta$
ρ_2	$26.60 \sigma_\theta$	—	$25.8 \sigma_\theta$
ρ_3	$27.75 \sigma_\theta$	—	$27.75 \sigma_\theta$
γ_2	1.57	1.91	1.69
$2\pi/l$	300 km	—	1200 km

Assuming U_n to be meridionally uniform, q_n and the meridional gradient of Π_n are related to the other model variables as follows:

$$q_n = \nabla^2 \phi_n + \frac{(-1)^n}{\gamma_2 \delta_n \lambda^2} (\phi_1 - \phi_2 - \gamma_n \phi_2) \quad (3)$$

and

$$\Pi_{ny} = \beta - \frac{(-1)^n}{\gamma_2 \delta_n \lambda^2} (U_1 - U_2 - \gamma_n U_2), \quad (4)$$

where

$$\delta_n = \frac{H_n}{H_2}, \quad \gamma_n = \frac{\rho_n - \rho_1}{\rho_3 - \rho_2}, \quad \text{and} \quad (5)$$

$$\lambda^2 = \frac{(\rho_3 - \rho_2)gH_2}{\rho_0 f_0^2}.$$

In the above equations, ∇^2 denotes the horizontal Laplacian operator, H_n is the mean thickness of layer n , ρ_n is the density of layer n , β is the meridional gradient of the Coriolis parameter, f_0 is the Coriolis parameter at the reference latitude, and ρ_0 is the reference density. Defined as in Eq. (5), δ_2 gives the layer depth ratio, γ_2 is the stratification ratio, and λ is the internal Rossby radius of deformation.

The stability of the vertically sheared STCC–SEC system can be analyzed by seeking the normal mode solution: $\phi_n = \text{Re}[A_n \expi(kx + ly - kct)]$. Substituting ϕ_n into Eq. (2) and requiring nontrivial solutions for A_n leads to the following quadratic equation for the complex phase speed $c = c_r + ic_i$:

$$Rc^2 - (U_1 R + U_2 R - P\Pi_{2y} - Q\Pi_{1y})c + (U_1 U_2 R + \Pi_{1y} \Pi_{2y} - U_1 P\Pi_{2y} - U_2 Q\Pi_{1y}) = 0, \quad (6)$$

where

$$P = K^2 + 1/\gamma_2 \delta_1 \lambda^2, \quad Q = K^2 + (1 + \gamma_2)/\gamma_2 \lambda^2,$$

and

$$R = PQ - 1/\gamma_2^2 \delta_1 \lambda^4.$$

For the STCC–SEC system with $U_1 - U_2 > 0$ (i.e., $\Pi_{1y} > 0$), it is possible to show that the necessary and sufficient condition for instability is $\Pi_{2y} < 0$, or

$$U_1 - U_2 > \gamma_2 \lambda^2 \beta + \gamma_2 U_2 \quad (7)$$

(see the appendix). Notice that on the rhs of Eq. (7), $\gamma_2 \lambda^2 \beta \equiv (\rho_2 - \rho_1)gH_1\beta/\rho_0 f_0^2$, is a measure of the baroclinic Rossby wave speed in the 2½-layer system. Physically, Eq. (7) indicates that the vertical shear has to exceed the local baroclinic Rossby wave speed, augmented by $\gamma_2 U_2$, in order for the system to become baroclinically unstable.

In Table 1, we list the parameter values appropriate for the STCC–SEC system in August and May, respectively. The reference latitude for f_0 and β is taken at 25°S and the other parameter values are estimated from the monthly climatological data sets of Conkright et al. (2002). The differences between the August and May conditions reside in two parameters: U_1 and γ_2 . In August when surface cooling prevails over the Southern Hemisphere ocean, the STCC velocity U_1 is larger and the stratification parameter γ_2 is smaller. As can easily be verified in Eq. (7), both a larger U_1 and a smaller γ_2 strengthen the baroclinic instability potential in the 2½-layer system. In Fig. 7, we plot the phase speed (c_r) and the growth rate (kc_i) of the STCC–SEC system as a function of k using the parameters listed in Table 1. Although the system is unstable under both the August (solid lines) and May (dashed line) conditions, the growth rates between the two cases are substantially different. The most unstable mode in August has $kc_i = 0.0123 \text{ day}^{-1}$, or an e -folding time scale of 81 days; in contrast, the e -folding time scale for the most unstable mode in May is $O(200 \text{ days})$. This seasonal difference in the intensity of the baroclinic instability likely explains the seasonal modulation in the EKE field observed in the STCC–SEC system. In addition, the observed lag between the maximum shear in August and the EKE maximum in November–December is consistent with the 81 day e -folding time calculated above.

In concluding this section, we note that while the EKE signal has a well-defined annual cycle, Fig. 6 reveals that the zonal velocity shear between the STCC and the

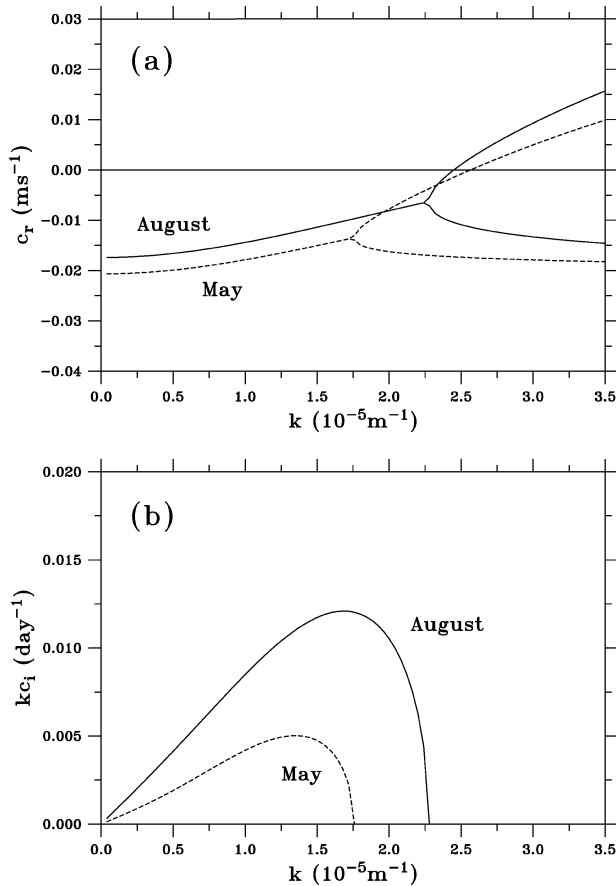


FIG. 7. (a) Phase speed and (b) growth rate as a function of zonal wavenumber k for the vertically sheared STCC–SEC system. Solid lines are the results for Aug and dashed lines for May. Parameter values appropriate for Aug and May are listed in Table 1.

subsurface SEC inferred from the climatological data also shows a subannual variation. A secondary maximum in $U_1 - U_2$ is seen around January. The reason for this secondary maximum’s existence is unclear. The regional atmospheric forcing (i.e., the Ekman flux convergence and the latitude-dependent surface heat flux forcing) all have well-defined annual cycles that are consistent with generating the August $U_1 - U_2$ maximum, but not the secondary peak around January. Given that the zonal velocity shear in the NPSTCC–NEC system of the North Pacific has a well-defined annual cycle and that the STCC–SEC and the NPSTCC–NEC systems share similar formation mechanisms, we suspect that the lack of a purely annual cycle in $U_1 - U_2$ in the STCC–SEC system (the solid line in Fig. 6) could result from insufficient hydrographic measurements in the South Pacific Ocean. Clearly, future studies are needed to supplement the monthly temperature–salinity (T – S) climatology of Conkright et al. (2002) and better describe the seasonally varying mean state of the STCC–SEC system.

4. SECC as a baroclinic zonal jet

In the introduction, we noted that the high EKE band along 9°S in the western South Pacific coincides with the path of the eastward-flowing SECC. A look at the mean flow pattern in Fig. 3 indicates that like the STCC–SEC system in the subtropical gyre, the climatological mean SECC is also underlain by the westward-flowing SEC. Although this suggests that baroclinic instability may be a valid mechanism to also explain the EKE signals in the SECC band, two important differences exist between the STCC–SEC and the SECC–SEC systems.

The first is that while the westward-flowing SEC underneath the STCC is seasonally constant, the subsurface SEC below the SECC varies considerably with seasons. Figure 8 compares the monthly zonal flow patterns of the SECC–SEC system (averaged from 170°E to 180°) in March, June, September, and December. In March when the regional EKE level is relatively high, the surface SECC jet is more intense and its presence can be seen to extend deep into the subsurface layer. The westward-flowing SEC prevails underneath the STCC only in the austral summer months when the surface SECC jet becomes weak (Figs. 8c,d). The second, and dynamically more significant, difference is that the SECC–SEC system exists in the lower latitude (~9°S) where the baroclinic Rossby wave speed is faster. Both of these effects increase the rhs of Eq. (7), increasing the shear and the value of U_1 required for baroclinic instability.

Using the parameter values appropriate for the SECC–SEC system in March (see column 4 in Table 1), we find that the baroclinic Rossby wave speed $\gamma_2 \lambda^2 \beta$ is 0.42 m s⁻¹. Coupled with U_2 being positive, the condition in Eq. (7) indicates that U_1 has to exceed

$$\gamma_2 \lambda^2 \beta + (1 + \gamma_2) U_2 = 0.47 \text{ m s}^{-1}$$

in order for the system to become baroclinically unstable. In comparison with this minimally required U_1 value, Fig. 8a indicates that the maximum zonal SECC velocity is <0.20 m s⁻¹. One can certainly regard this monthly picture as underrepresenting the strength of the SECC either because of insufficient in situ measurements or because the observed flow pattern reflects the outcome of instability and is, therefore, necessarily weaker in intensity than the *true* mean flow state. Nevertheless, the large discrepancy between the required and observed U_1 values suggests that the baroclinic instability is not a likely mechanism to account for the high eddy variability detected in the SECC band.

5. SECC as a barotropic zonal jet

Instead of the vertical shear in the mean flow, we will consider in this section the horizontal shear of the SECC–SEC system as a source of the observed eddy signals. Strong horizontal shear between the eastward-

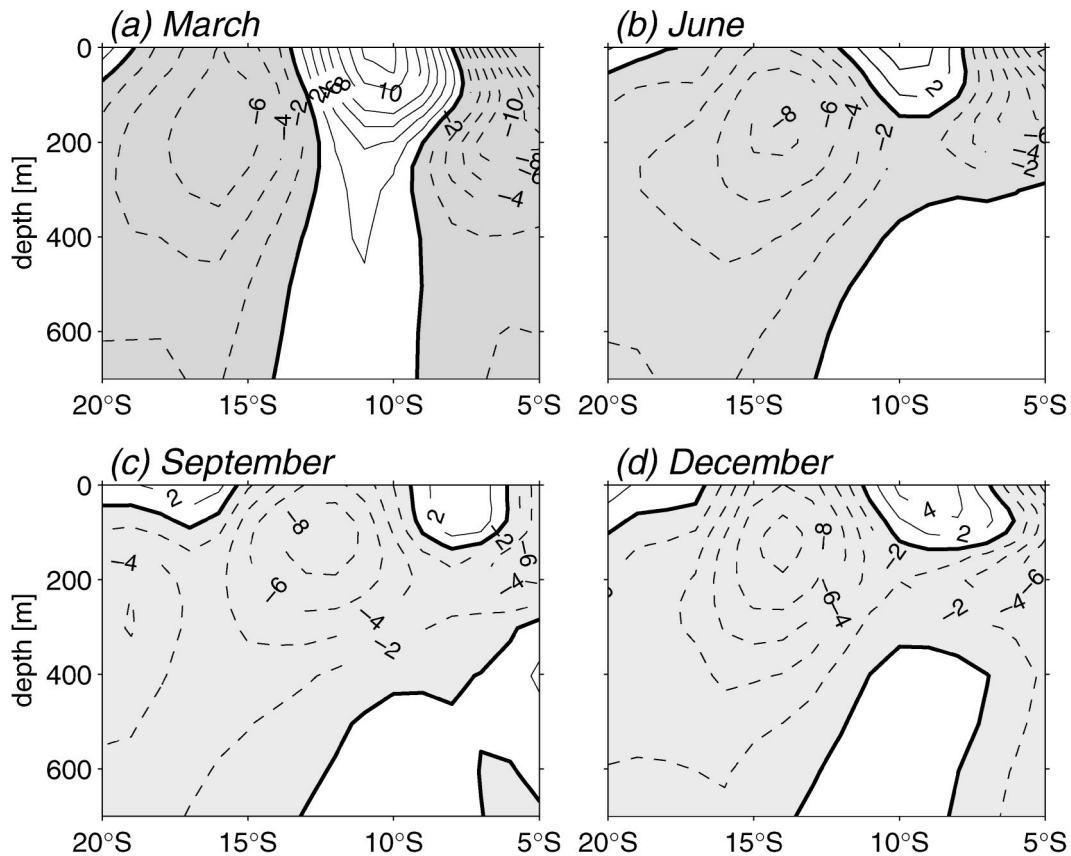


FIG. 8. Geostrophic zonal flow patterns in (a) Mar, (b) Jun, (c) Sep, and (d) Dec averaged from 170°E to 180°. The geostrophic flows are calculated from the monthly mean temperature and salinity data sets of WOA01 (Conkright et al. 2002) with a reference level at 1500 dbar. Contour units are centimeters per second.

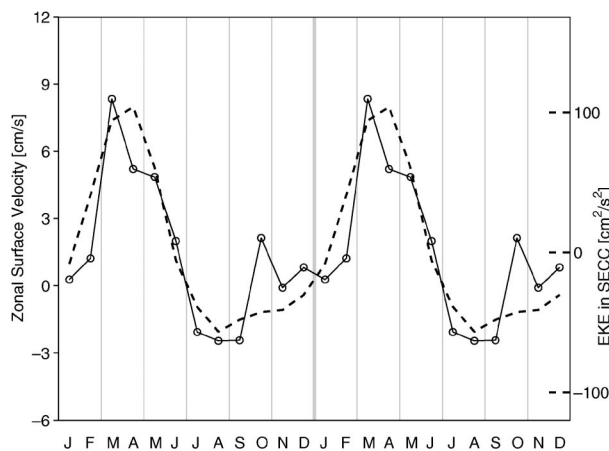


FIG. 9. Surface geostrophic zonal flow averaged in the SECC region of 13°–8°S and 170°E–180° (solid line). The zonal flow is calculated from the monthly mean temperature and salinity data sets of WOA01 (Conkright et al. 2002). The dashed line shows the monthly eddy kinetic energy time series in the SECC region (same as the solid line in Fig. 5a).

flowing SECC and its flanking westward-flowing SECC can be easily discerned in the zonal mean flow patterns shown in Figs. 3 and 8. Notice that while the strength of the SECC remains relatively constant, Fig. 8 reveals that the intensity of the SECC changes considerably with seasons. As plotted in Fig. 9 (solid line), the SECC jet reaches its maximum in March and weakens gradually to a minimum in August. This annual cycle in the strength of the SECC jet leads the seasonal EKE signals by ~ 1 month (cf. the dashed line in Fig. 9).

In order to examine how the horizontal shear of the SECC–SEC system may contribute to the observed EKE signals, we adopt below a $1\frac{1}{2}$ -layer reduced-gravity model that has a mean sheared flow $U(y)$ in its active upper layer. The linearized momentum and continuity equations governing the velocity (\mathbf{u}) and upper layer thickness (h) perturbations in this model are

$$\frac{\partial \mathbf{u}}{\partial t} + U \frac{\partial \mathbf{u}}{\partial x} + v \frac{\partial U}{\partial y} \mathbf{i} + f \mathbf{k} \times \mathbf{u} = -g' \nabla h \quad (8)$$

$$\frac{\partial h}{\partial t} + U \frac{\partial h}{\partial x} + v \frac{\partial H}{\partial y} + H \nabla \cdot \mathbf{u} = 0, \quad (9)$$

where g' is the reduced gravity constant, v is the anom-

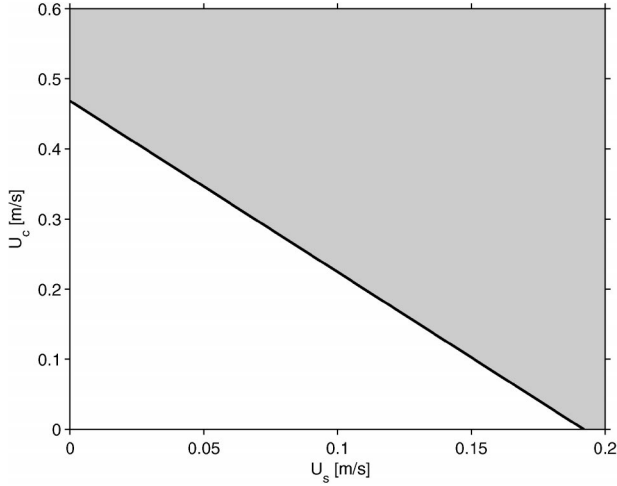


FIG. 10. Neutral stability line separating the barotropically stable (unshaded) and unstable (shaded) regions. The line is given by Eq. (14) with external parameters appropriate for the SECC–SEC system: $\beta = 2.27 \times 10^{-11} \text{ m}^{-1} \text{ s}^{-1}$, $a = 120 \text{ km}$, and $\lambda = 120 \text{ km}$.

alous meridional velocity, and $H(y)$ is the mean upper layer thickness, which is in geostrophic balance with $U(y)$ through $fU = -g'H_y$. These governing equations can be combined to form the potential vorticity equation:

$$\left(\frac{\partial}{\partial t} + U\frac{\partial}{\partial x}\right)q + v\frac{\partial \Pi}{\partial y} = 0, \quad (10)$$

where

$$\Pi = \frac{f - U_y}{H} \quad \text{and} \quad q = \frac{1}{H}\left(\frac{\partial v}{\partial x} - \frac{\partial u}{\partial y}\right) - \frac{h}{H}\Pi$$

are the mean and perturbation potential vorticities, respectively. Using the quasigeostrophic approximation to relate \mathbf{u} to h (i.e., $f\mathbf{k} \times \mathbf{u} = -g'\nabla h$), we can again seek the normal-mode solution $h = \text{Re}[A \exp i(kx - kct)]$. Upon substitution into Eq. (10), we have

$$A_{yy} - (k^2 + \lambda^{-2})A + \frac{\beta - U_{yy} + U\lambda^{-2}}{U - c}A = 0, \quad (11)$$

where $\lambda^2 = g'H/f^2$ is the squared internal Rossby radius of deformation. As shown by Lipps (1963), a necessary condition for barotropic instability in this system is the change of sign in the gradient of the mean potential vorticity:

$$\Pi_y \propto \beta - U_{yy} + U\lambda^{-2}. \quad (12)$$

To study the stability of the horizontally sheared SECC–SEC system, we assume that the mean flow is comprised of a uniform westward-flowing SEC and a Gaussian-shaped, eastward-flowing SECC jet:

$$U(y) = -U_s + (U_c + U_s) \exp[-(y - y_0)^2/a^2], \quad (13)$$

where U_s denotes the speed of the SEC, y_0 is the center

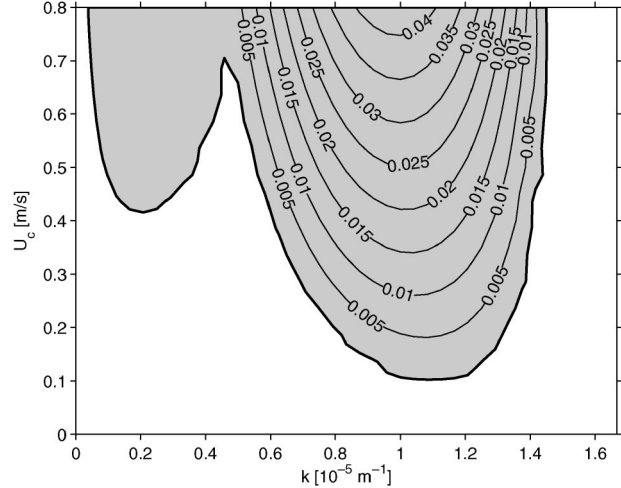


FIG. 11. Growth-rate dependence (day^{-1}) on U_c for the horizontally sheared SECC–SEC system. The mean flow profile is given by Eq. (13), where $U_s = 0.15 \text{ m s}^{-1}$, $y_0 = 0$, and $a = 120 \text{ km}$. Shaded areas denote the barotropically unstable domain.

latitude of the SECC jet, U_c is its maximum eastward velocity, and a is its e -folding width scale. Given the mean flow profile in Eq. (13), the necessary condition for instability is satisfied when the maximum eastward speed of the jet U_c exceeds a threshold value:

$$U_c > \left(\beta - \frac{U_s}{\lambda^2}\right)\frac{a^2}{4} \exp\left(\frac{3}{2} + \frac{a^2}{4\lambda^2}\right) - U_s. \quad (14)$$

In Fig. 10, we plot this threshold value as a function of the speed of the background westward flow, U_s . Parameter values for β , λ , and a have been chosen to be appropriate for the SECC–SEC system: $\beta = 2.27 \times 10^{-11} \text{ s}^{-1} \text{ m}^{-1}$, $a = 120 \text{ km}$, and $\lambda = 120 \text{ km}$ (Chelton et al. 1998). Presence of the background westward flow (i.e., the SEC) can significantly lower the threshold for barotropic instability. For typical values of $U_s = 0.10$ – 0.15 m s^{-1} , for example, the threshold U_c value reduces from 0.47 m s^{-1} when $U_s = 0$ to 0.10 – 0.22 m s^{-1} . [Notice that the threshold U_c value of 0.47 m s^{-1} here is from Eq. (14) and should not be confused with the baroclinic instability threshold value presented in section 4.] Physically, the presence of the background westward flow decreases the planetary β effect that stabilizes the sheared zonal flow (see Philander 1976). As easily seen in Eq. (14), the “effective” β in the presence of U_s is $\beta - U_s/\lambda^2$.

To further examine the stability properties of the horizontally sheared SECC–SEC system, we solved Eq. (11) numerically by regarding c as an eigenvalue. Figure 11 shows the growth rate kc_i dependence on the eastward speed of the SECC jet, U_c . For external parameters, $U_s = 0.15 \text{ m s}^{-1}$ and β , λ , and a are set the same as for Fig. 10. The minimally required U_c value for instability shown in Fig. 11 is 0.10 m s^{-1} , which matches the threshold U_c value derived from the necessary

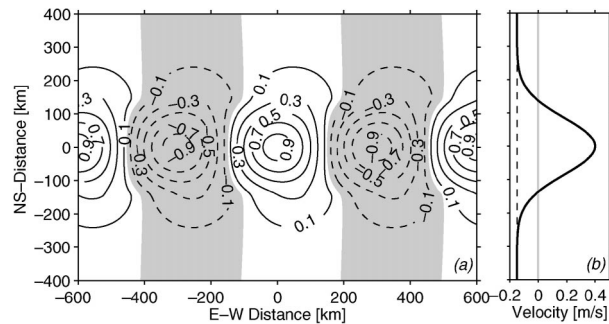


FIG. 12. (a) Upper-layer thickness anomaly pattern of the most unstable wave when the horizontally sheared SECC–SEC system $U(y)$ is given by Eq. (13) with $U_s = 0.15 \text{ m s}^{-1}$, $U_c = 0.40 \text{ m s}^{-1}$, $y_0 = 0$, and $a = 120 \text{ km}$ [see (b)]. Shaded areas denote negative anomalies. Zonal wavenumber k is $1.04 \times 10^{-5} \text{ m}^{-1}$ (see Fig. 11).

condition (cf. Fig. 10).² In comparison with the baroclinic case in which $(U_1)_{\min} = 0.47 \text{ m s}^{-1}$, this required magnitude for the SECC jet speed is much lower. In Fig. 12, we plot the spatial distribution of the upper-layer thickness perturbations for the most unstable wave when $U_c = 0.40 \text{ m s}^{-1}$. Not surprisingly, the perturbations are confined to the band where the eastward SECC jet is located. The tilt of the perturbation phase lines relative to the horizontal shear of the mean flow is characteristic of barotropic instability.

For the case of $U_c = 0.40 \text{ m s}^{-1}$, Fig. 11 shows that the e -folding time scale for the most unstable wave is ~ 52 days. Like the baroclinic instability case considered in section 3, the growth rate for the unstable waves in the barotropic case also depends sensitively on the speed of the surface mean flow. When U_c is reduced to 0.20 m s^{-1} , for example, the e -folding scale increases to ~ 200 days. In contrast with the horizontally averaged current values needed to predict baroclinic instability, the peak value (U_c) required to estimate the appropriate horizontal shear profile is more difficult to deduce from a climatological dataset. Given the relatively simple velocity profile of Eq. (13) used to represent the SECC–SEC system, it is probably unproductive to speculate the exact values of U_s and U_c appropriate for the SECC–SEC system. Instead, we will focus below on whether the observational result is consistent with the notion that barotropic instability is responsible for seasonally modulating EKE levels in the SECC region.

From the equation governing the evolution of the EKE, one can define the barotropic conversion rate (BCR) as follows:

$$\text{BCR} = \overline{u'u'}U_x + \overline{u'v'}(U_y + V_x) + \overline{v'v'}V_y, \quad (15)$$

where overbars denote temporal means, and primes the residuals from the mean. As discussed in detail in Qiu (1995) and in other studies referenced therein, a negative

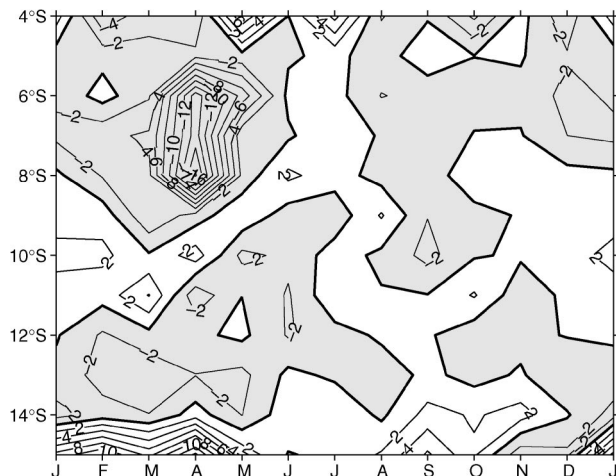


FIG. 13. Zonally averaged barotropic conversion rate [see Eq. (15)] between 165°E and 170°W as a function of month and latitude. Contour units: 10^{-6} m s^{-3} . Shaded areas denote negative BCR values, indicating conversion from the mean kinetic energy to eddy kinetic energy through barotropic instability.

BCR implies the energy transfer from the mean kinetic energy to the EKE and is indicative of barotropic instability of the mean flow system. Positive BCRs, on the other hand, suggest energy transfer to the mean flow at the expense of the EKE. To evaluate the BCRs from the altimeter-derived SSH data, we first high-pass filtered the SSH anomaly data with a half-power point at 180 days. This filtering enables the resulting (u', v') signals to represent largely the mesoscale eddy signals. From the filtered (u', v') field, we calculate their auto- and cross-covariances on a monthly basis and combine them with the monthly mean surface (U, V) field estimated from the climatological T – S dataset of Conkright et al. (2002) as in Eq. (15). Figure 13 shows the zonally averaged BCR values between 165°E and 170°W as a function of month and latitude. During most of the year, the estimated BCRs are negative in the band from 5° to 14°S , indicating the sheared SECC–SEC system is barotropically unstable. The maximum energy conversion occurs in April, one month after the SECC jet reaches its seasonal maximum in March (cf. Fig. 9). Like the STCC–SEC case considered in section 3, this delay can be interpreted as the time required by the barotropic instability in the sheared SECC–SEC system to fully develop. The above analysis of energetics, thus, supports the notion that the SECC–SEC is a barotropically unstable system and that the seasonally varying strength of this instability (due to the seasonal changes in the intensity of the SECC jet) gives rise to the seasonally modulating EKE signals detected by the satellite measurements.

6. Summary

Decade-long satellite altimeter data from the T/P and *ERS-1/2* missions are used to investigate the eddy ki-

² With $U(y)$ being axisymmetric, the necessary condition requiring the change of sign in the mean potential vorticity also serves as the sufficient condition. See Drazin and Reid (1981, chapter 22) for proof.

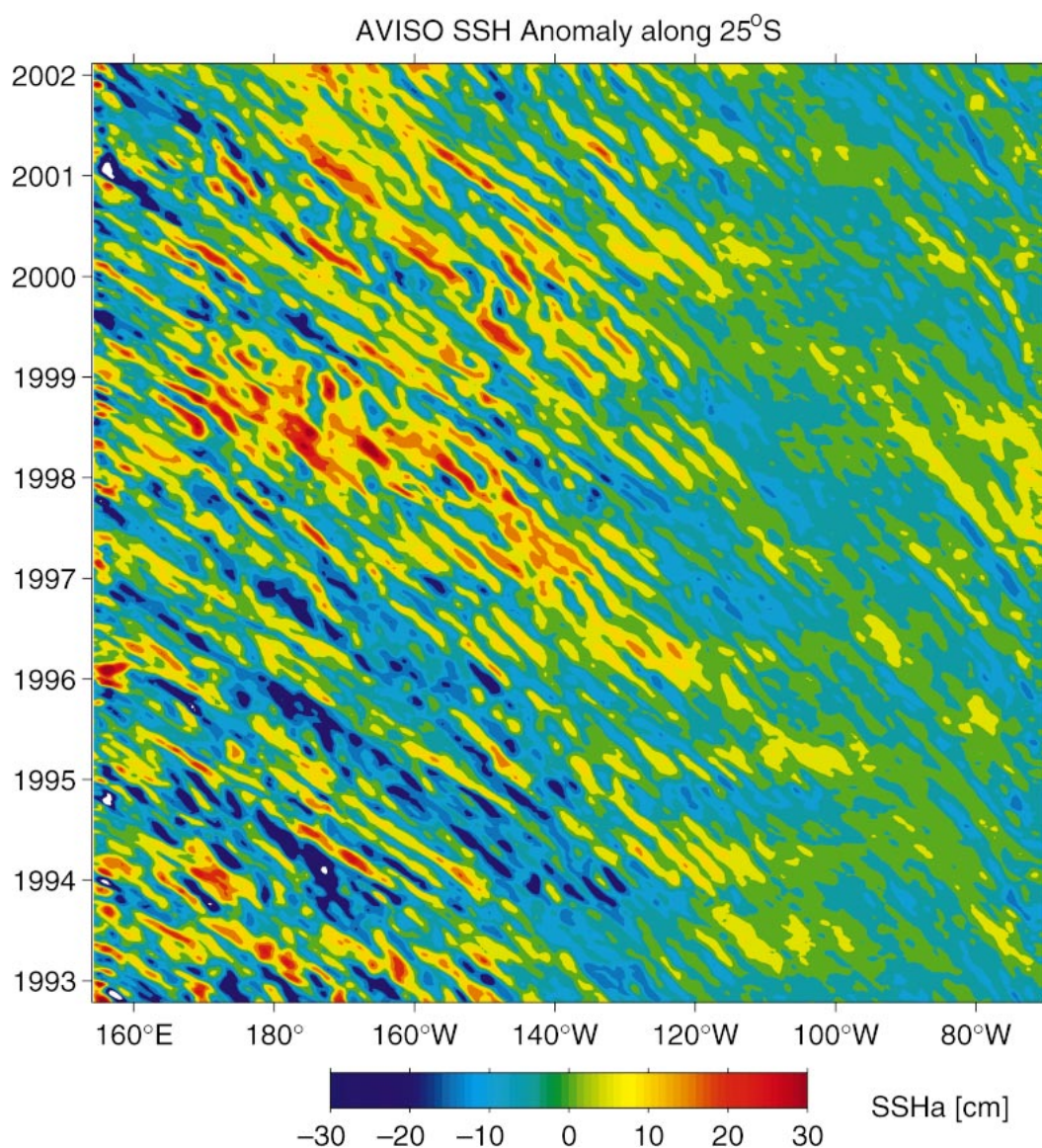


FIG. 14. Time-longitude plot of the SSH anomalies along 25°S in the South Pacific Ocean.

netic energy signals in the South Pacific Ocean. The study has focused on two eastward-flowing surface current bands where the EKE levels are high and their seasonal modulations are highly regular.

The first band is located at 21°–29°S along the path of the South Tropical Countercurrent. Despite being a relatively weak surface current near the center of the wind-driven subtropical gyre, the eastward-flowing STCC is underlain by the westward-flowing South Equatorial Current. This causes the mean potential vorticity gradient in the subsurface layer to have an opposite sign (i.e., negative) from that in the surface STCC layer, rendering the vertically sheared STCC–SEC system to be baroclinically unstable. Although the instability criterion is satisfied year-round, comparing the parameter values appropriate for the mean state in dif-

ferent seasons reveals that the August (i.e., the Southern Hemisphere winter) condition is considerably more favorable for baroclinic instability than the summer and fall conditions. In August, latitudinally dependent surface cooling not only increases the vertical velocity shear between the STCC and SEC, it also reduces the density jump between the surface and subsurface layers. Both of these effects enhance the growth of the baroclinic instability. The maximum growth rate for the STCC/SEC system in August is estimated to be $O(80)$ days). In contrast, the seasonal heating over the southern hemisphere summer and fall weakens the STCC–SEC shear and increases the density jump between the STCC and SEC layers. The typical growth rate, for example, exceeds 200 days under the May conditions. It is this seasonal difference in the intensity of baroclinic insta-

bility that modulates the eddy kinetic energy level detected in the STCC–SEC system. Unlike western boundary currents with more vigorous instability, the growth rate for the STCC–SEC system even under the August conditions is on the order of several months. This likely explains the long time lag between the maximum STCC–SEC’s shear in August and the peak eddy kinetic energy level in November and December.

The second high EKE band is located along the path of the South Equatorial Countercurrent centered near 9°S in the western equatorial South Pacific. Like the STCC in the subtropics, the SECC is similarly underlain by the westward-flowing SEC. However, with the local deformation radius being large, the vertically sheared SECC–SEC system is unable to reverse the sign of the mean potential vorticity gradient in the subsurface layer, making the baroclinic instability mechanism irrelevant for the observed high EKE signals. Focusing on the horizontal shear between the SECC and SEC, we found that the presence of the broad, westward-flowing SEC deepens (shoals) the thermocline to the south (north) and reduces the stabilizing effect of planetary β . Using an idealized velocity profile for the background mean flow and the parameter values appropriate for the SECC–SEC system, we found that the criterion for barotropic instability is satisfied, especially during the months of March through May when the wind-driven SECC is intense. We argued that the seasonally modulating EKE levels detected by the altimeter measurements are the manifestations of changes in the intensity of barotropic instability due to the seasonally varying horizontal shear between the SECC and SEC. This argument is consistent with an energetics analysis, in which we examined the time-varying barotropic conversion rates based on the available altimetric data.

In this study, we have focused on the seasonal eddy signals found in the STCC and SECC bands. In addition to the seasonal modulations, interannual EKE changes are also detected by the satellite altimeter measurements (recall Fig. 4). Future studies are clearly needed to clarify their underlying causes. The issue of how the unstable waves will evolve after the initial disturbances in the STCC–SEC and the SECC–SEC systems attain finite amplitudes is not addressed in this study. Previous studies by Rhines (1977) and Halliwell et al. (1994) suggest that the unstable waves will evolve into eddies whose length scales tend to increase through nonlinear cascade processes. The cascade processes are shown to cease when the eddies become large enough to disperse as baroclinic Rossby waves. Indeed, the presence of westward-propagating, wavelike anomalies within the STCC region is well captured by SSH measurements (see Fig. 14). Future studies are needed to further clarify the nonlinear interactions of these waves and to examine their impact upon the time-dependent circulations along the western boundary of the South Pacific Ocean.

Acknowledgments. This study benefited from fruitful discussions with Ted Durland, Steve Chiswell, and Billy Kessler. Detailed comments made by the anonymous reviewers helped improve an early version of the manuscript. The merged T/P and ERS-1/2 altimeter data are provided by the CLS Space Oceanography Division as part of the Environment and Climate EU ENACT project and with support from CNES. Support from NASA through Contracts 1207881 and 1228847 is gratefully acknowledged.

APPENDIX

Conditions for Instability in a 2½-Layer Model

From the dispersion relation Eq. (6), instability of the system is assured when c has complex conjugate roots, that is, when the radicant of the equation,

$$\begin{aligned} \Delta &= (U_1 R + U_2 R - P \Pi_{2y} - Q \Pi_{1y})^2 \\ &\quad - 4R(U_1 U_2 R + \Pi_{1y} \Pi_{2y} - U_1 P \Pi_{2y} - U_2 Q \Pi_{1y}) \\ &= (U_s R + P \Pi_{2y} - Q \Pi_{1y})^2 + \Pi_{1y} \Pi_{2y} / \gamma_2^2 \delta_1 \lambda^4, \end{aligned} \quad (\text{A1})$$

becomes negative, where $U_s \equiv U_1 - U_2$. For $U_s > 0$, Π_{1y} is by definition positive, and the *necessary* condition for $\Delta < 0$ can easily be verified from Eq. (A1) to be $\Pi_{2y} < 0$. With the use of Eq. (4), this leads to

$$U_s > \gamma_2 \lambda^2 \beta + \gamma_2 U_2. \quad (\text{A2})$$

To prove that Eq. (A2) also constitutes the *sufficient* condition for baroclinic instability, let us consider the neutral wave solution, $\Delta = 0$. The minimum U_s is attainable by solving $\partial \Delta / \partial K^2 = 0$. Recognizing $\partial U_s / \partial K^2 = 0$ (and hence, $\partial \Pi_{ny} / \partial K^2 = 0$) at the point $U_s = (U_s)_{\min}$ and setting $\partial \Delta / \partial K^2 = 0$, we find

$$\begin{aligned} &(U_s R + P \Pi_{2y} - Q \Pi_{1y}) \\ &\quad \times \left(U_s \frac{\partial R}{\partial K^2} + \Pi_{2y} \frac{\partial P}{\partial K^2} - \Pi_{1y} \frac{\partial Q}{\partial K^2} \right) = 0. \end{aligned} \quad (\text{A3})$$

Because the solution from $U_s \partial R / \partial K^2 + \Pi_{2y} \partial P / \partial K^2 - \Pi_{1y} \partial Q / \partial K^2 = 0$ cannot simultaneously satisfy $\Delta = 0$, the condition for finding $(U_s)_{\min}$ reduces to

$$U_s R + P \Pi_{2y} - Q \Pi_{1y} = 0. \quad (\text{A4})$$

Combining Eqs. (A4) and (A1), we have $\Pi_{2y} [(U_s)_{\min}] = 0$, or

$$(U_s)_{\min} = \gamma_2 \lambda^2 \beta + \gamma_2 U_2. \quad (\text{A5})$$

This minimum shear is exactly the shear required by the necessary condition Eq. (A2). In other words, for $U_s > 0$, Eq. (A2) serves as the *sufficient* condition for baroclinic instability of the system as well.

REFERENCES

- Chelton, D. B., R. A. de Szoeke, M. G. Schlax, K. E. Naggar, and N. Siwertz, 1998: Geographical variability of the first baroclinic Rossby radius of deformation. *J. Phys. Oceanogr.*, **28**, 433–460.

- Conkright, M. E., R. A. Locarnini, H. E. Garcia, T. D. O'Brien, T. P. Boyer, C. Stephens, and J. I. Antonov, 2002: *World Ocean Atlas 2001: Objective Analyses, Data Statistics, and Figures, CD-ROM Documentation*. National Oceanographic Data Center, 17 pp. [Available online at <http://www.nodc.noaa.gov/OC5/WOA01/readme.pdf>.]
- Delcroix, T., G. Eldin, and C. Hémin, 1987: Upper ocean water masses and transports in the western tropical Pacific (165°E). *J. Phys. Oceanogr.*, **17**, 2248–2262.
- de Szoeke, R. A., 1987: On the wind-driven circulation of the South Pacific Ocean. *J. Phys. Oceanogr.*, **17**, 613–630.
- Drazin, P. G., and W. H. Reid, 1981: *Hydrodynamic Stability*. Cambridge University Press, 527 pp.
- Ducet, N., and P.-Y. Le Traon, 2001: A comparison of surface eddy kinetic energy and Reynolds stresses in the Gulf Stream and the Kuroshio Current systems from merged TOPEX/Poseidon and ERS-1/2 altimetric data. *J. Geophys. Res.*, **106**, 16 603–16 622.
- Fu, L.-L., and A. Cazenave, Eds., 2001: *Satellite Altimetry and Earth Sciences*. Academic Press, 463 pp.
- Gouriou, Y., and J. Toole, 1993: Mean circulation of the upper layers of the western equatorial Pacific Ocean. *J. Geophys. Res.*, **98**, 22 495–22 520.
- Halliwel, G. R., Jr., G. Peng, and D. B. Olson, 1994: Stability of the Sargasso Sea subtropical frontal zone. *J. Phys. Oceanogr.*, **24**, 1166–1183.
- Huang, R. X., and B. Qiu, 1998: The structure of the wind-driven circulation in the subtropical South Pacific. *J. Phys. Oceanogr.*, **28**, 1173–1186.
- Kessler, W. S., and B. A. Taft, 1987: Dynamic heights and zonal geostrophic transports in the central tropical Pacific during 1979–84. *J. Phys. Oceanogr.*, **17**, 97–122.
- Le Traon, P.-Y., and F. Ogor, 1998: ERS-1/2 orbit improvement using TOPEX/Poseidon: The 2 cm challenge. *J. Geophys. Res.*, **103**, 8045–8057.
- , F. Nadal, and N. Ducet, 1998: An improved mapping method of multisatellite altimeter data. *J. Atmos. Oceanic Technol.*, **15**, 522–534.
- Lipps, F. B., 1963: Stability of jets in a divergent barotropic fluid. *J. Atmos. Sci.*, **20**, 120–129.
- Merle, J., H. Rotschi, and B. Voituriez, 1969: Zonal circulation in the tropical western South Pacific at 170°E. *Bull. Jpn. Soc. Fish. Oceanogr.*, Special Issue (Prof. Uda's Commemorative Papers), 91–98.
- Morris, M., D. Roemmich, and B. Cornuelle, 1996: Observations of variability in the South Pacific subtropical gyre. *J. Phys. Oceanogr.*, **26**, 2359–2379.
- Pedlosky, J., 1987: *Geophysical Fluid Dynamics*. Springer-Verlag, 710 pp.
- Philander, S. G. H., 1976: Instabilities of zonal equatorial currents. *J. Geophys. Res.*, **81**, 3725–3735.
- Qiu, B., 1995: Variability and energetics of the Kuroshio Extension and its recirculation gyre from the first two-year TOPEX data. *J. Phys. Oceanogr.*, **25**, 1827–1842.
- , 1999: Seasonal eddy field modulation of the North Pacific Subtropical Countercurrent: TOPEX/Poseidon observations and theory. *J. Phys. Oceanogr.*, **29**, 2471–2486.
- Reid, J. L., 1959: Evidence of a South Equatorial Countercurrent in the Pacific Ocean. *Nature*, **184**, 209–210.
- Rhines, P. B., 1977: The dynamics of unsteady currents. *The Sea*, E. D. Goldberg et al., Eds., *Marine Modeling*, Vol. 6, John Wiley and Sons, 189–318.
- Roemmich, D., and B. Cornuelle, 1990: Observing the fluctuations of gyre-scale ocean circulation: A study of the subtropical South Pacific. *J. Phys. Oceanogr.*, **20**, 1919–1934.
- , and P. Sutton, 1998: The mean and variability of ocean circulation past northern New Zealand: Determining the representativeness of hydrographic climatologies. *J. Geophys. Res.*, **103**, 13 041–13 054.
- Rotschi, H., 1973: Hydrography at 170°E in the South Pacific. *Oceanography of the South Pacific 1972*, R. Fraser, Ed., New Zealand National Commission for UNESCO, 113–128.
- Stanton, B., J. H. Sutton, and S. M. Chiswell, 1997: The East Auckland Current, 1994–95. *N. Z. J. Mar. Freshwater Res.*, **31**, 537–549.
- Tomczak, M., and J. S. Godfrey, 1994: *Regional Oceanography: An Introduction*. Pergamon, 422 pp.
- Tsuchiya, M., 1968: *Upper Waters of the Intertropical Pacific Ocean*. Johns Hopkins Oceanographic Studies, Vol. 4, Johns Hopkins Press, 50 pp.
- Yoshida, K., and T. Kidokoro, 1967: A subtropical countercurrent (II)—A prediction of eastward flows at lower subtropical latitudes. *J. Oceanogr. Soc. Japan*, **23**, 231–246.